Plasmonics (2018) 13:2249–2254
https://doi.org/10.1007/s11468-018-0745-z

Light Funneling Profile During Enhanced Transmission Through a Subwavelength Metallic Slit

Jing-Wei Li[1] · Jian-Shiung Hong[1] · Wei-Ting Chou[1] · Ding-Jie Huang[1] · Kuan-Ren Chen[1]

Received: 28 December 2017 / Accepted: 13 March 2018 / Published online: 26 March 2018

Abstract
The funneling profile of enhanced light transmission through a subwavelength slit in a perfect electric conductor is studied with finite-difference time-domain simulation. From the wave-charge interaction dynamics, it is found that the EM wave energy is funneled while charges are accumulated at the edges of the slit. The Poynting vector indicates a boundary within which the wave energy flows toward the slit. Therefore, a funneling profile is defined by this boundary; as the slit width and thickness determine the transmitted energy density, the size of the funneling area is a relevant quantity of major concern.

Keywords Subwavelength slit · Light funneling · Fabry-Pérot resonance

Introduction

In the recent decades, the extraordinary optical transmission (EOT) through a subwavelength metallic nanostructure [1] has drawn significant attentions due to its capability of controlling the electromagnetic (EM) wave in both the spectral [2–4] and spatial domains [5–11]. Many potential applications, such as bio-sensing [12], optical antennas [13], plasmonic lithography [14], and color filters [15, 16], have thus been proposed.

The enhancement of transmission through various configurations was extensively studied to understand the underlying physics, such as a single aperture/slit [17–25], aperture/slit array [2, 4, 26–29], aperture/slit surrounded by grooves [3, 6, 7, 10, 11, 30–33], or particular composite structures [8, 9, 34, 35]. Besides the excitation of surface plasmons and the Fabry-Pérot resonance [18], the light funneling effect [17, 23–26, 36] was believed to be the more fundamental mechanism and could be exploited for the extensive light control [37–39]. This effect utilizes the charges accumulated at a discontinuous surface [40, 41] when illuminated and draws the nearby wave energy due to the diffraction [42]. Therefore, the effect is intrinsic to the structure and does not require the plasmonic coupling. A single slit in a film of perfect electric conductor (PEC) was shown to have the capability of enhancing the optical transmission [17]. The coupling between a slit and the grooves surrounded [30], a composite aperture and slit array [34], a metallic slit combined with epsilon-near-zero materials [43], etc., could further enhance the funneling capability.

The study of the funneled energy flow should help us gain more insight into the enhanced light transmission; however, it has been rarely investigated [42]. To characterize the funneling and its profile, the interaction of a *p*-polarized incident wave with a subwavelength slit in a PEC film is studied. With the finite-difference time-domain (FDTD) simulation, the instant EM fields and Poynting vector show the light funneling and its mechanism. A boundary is defined to indicate the area where the energy flows toward the slit. The time-averaged Poynting vector further verifies the existence of the boundary. As the slit width and thickness determine the transmitted energy density, we will show that the size of the funneling area is positively correlated.

Section II introduces the funneling of light into a subwavelength slit from the FDTD simulation. The boundary of the funneling profile defined by the obtained Poynting vector is also presented. The funneling into a slit of various widths and finite thicknesses are proposed in sections III and IV, respectively. Section V is a summary.

✉ Kuan-Ren Chen
chenkr@phys.ncku.edu.tw

[1] Department of Physics, National Cheng Kung University, 1 University Road, Tainan 70101, Taiwan, Republic of China

Funneling of Light into a Subwavelength Slit

In this article, we consider a subwavelength slit of width $w = 80$ nm that is placed in the midst of a PEC film, as

shown in Fig. 1. A p-polarized plane wave of wavelength $\lambda = 640$ nm is incident; the source plane is one λ away from the film.

In the two-dimensional FDTD simulation, the cell size of the system of both directions is 2.5 nm and the system size is 30×3 μm^2. The time step of updating the EM field is 0.001 T (T is the period of the incident wave), and the time step of diagnosing is 0.01 T. The PEC film is simulated with the Drude model with the plasma frequency $\omega_p = 1.0 \times 10^{30}$ Hz and zero damping coefficient. Perfectly matched layers (PMLs) are employed as the boundary conditions. The electric field amplitude of the incident wave is 1 V/m. The impedance of vacuum is normalized to unity so that the magnetic field amplitude of the incident wave is also normalized to unity.

In our simulation, we let the film thickness h to be large enough, i.e., $h = 2$ μm, and let the diagnostic interval be from $t = 4\ T$ to $t = 5\ T$. In this case, the wave reflection from the exit of the slit is avoided. The light transmission through only the entrance of the slit can be obtained.

The instant EM fields from the simulation are shown in Fig. 2; simulated E_x field at $t = 4.22\ T$ is shown in Fig. 2a. At this instant, the tangential electric field of the incident wave at the metal surface ($y = 0$) is in the positive phase so that it drives the free electrons on the surface to move in the $-x$ direction as the $+J_x$ current and to let $E_x = 0$ at the surface. The current prevents the incident wave from penetration into the metal and then reflects the light in the direction opposite to that of the incidence. However, the current will not be continuous along the x direction near the slit; positive and negative charges are therefore accumulated at the left and right sides of the slit entrance, respectively, due to the conservation of the charges.

These accumulated charges form an electrical dipole [40] to diffract the light into the incident region ($y > 0$) and into the slit region ($y < 0$, $|x| < w/2$) as well. That is, the presence of the slit changes the direction of the incident energy flow in various angles. Since the slit width is much smaller than the wavelength, the diffracted wave is cylindrical in the incident region [44]. Besides the incident and reflected wave, the simulated E_x field above the slit, shown in Fig. 2a, is superposed by that of the diffracted cylindrical wave. In the slit region, the field amplitude measured at $y = -200$ nm is 1.367 in the case studied; the enhanced field indicates that the energy is concentrated toward the slit.

We show the H_z field at the same instant in Fig. 2b. The field above the slit is depressed because the magnetic field of the diffracted wave is destructive to those of the incident and reflected wave. Similar to the case of the E_x field, the field amplitude measured at $y = -200$ nm is also enhanced to 1.366. The E_y field is shown in Fig. 2c. The accumulated charges at the left and right sides of the slit entrance result in the positive and negative phase of the field close to the entrance, respectively. The field oscillates along the $\pm x$ direction, respectively, and quickly decays in the $+y$ direction.

The instant Poynting vector $\mathbf{S} = \hat{x}S_x + \hat{y}S_y$ is shown in Fig. 2c. Since $\mathbf{S} = \mathbf{E} \times \mathbf{H}$, we have $S_y = -E_xH_z$ and $S_x = E_yH_z$. The phases of the E_x and H_z fields above the slit are positive so that S_y is negative; it indicates the energy flows in the $-y$ direction. The magnitude of S_y decreases in the $+y$ direction since H_z is changing from the positive to the zero phase. The phases of the E_y field at the left and right entrance cause S_x to be positive and negative, respectively. That is, the energy around the slit flows into the slit as *the funneling effect*. Therefore, the transmission through the entrance is enhanced. Away from the entrance, while H_z in the x direction remains the same positive phase, the oscillation of the E_y field in the x direction changes the sign of S_x so that the energy becomes to flow outward. We find the locations around the slit where $S_x = 0$ along the x direction at every y to define the boundary of the funneling profile, as the dotted curve shown in Fig. 2c.

When the time increases to $t = 4.31\ T$, the E_x field is shown in Fig. 2d. The field of the positive phase shrinks and moves toward the slit while that of the negative phase is approaching. Figure 2e shows that the E_y field propagates in the $\pm x$ direction to have the larger area distribution. While the H_z field has the similar phase distribution to that in Fig. 2b (not shown), the Poynting vector as shown in Fig. 2e is therefore in the $+y$ direction, except that adjacent to the entrance. The boundary of the funneling profile as shown in Fig. 2e becomes wider but lower. The transmitted energy in the slit continues to propagate. At $t = 4.47\ T$, the zero phase of the E_x field is about to arrive at the entrance, as shown in Fig. 2f. The E_y field in Fig. 2g continues to

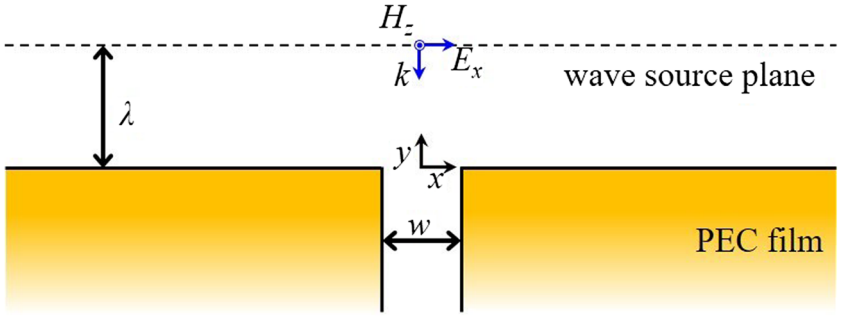

Fig. 1 Schematic of a subwavelength slit of width w in a PEC film. The film is illuminated by a p-polarized wave and its wavelength is $\lambda = 640$ nm. In the simulation, the wave source plane is located at one λ away from the film

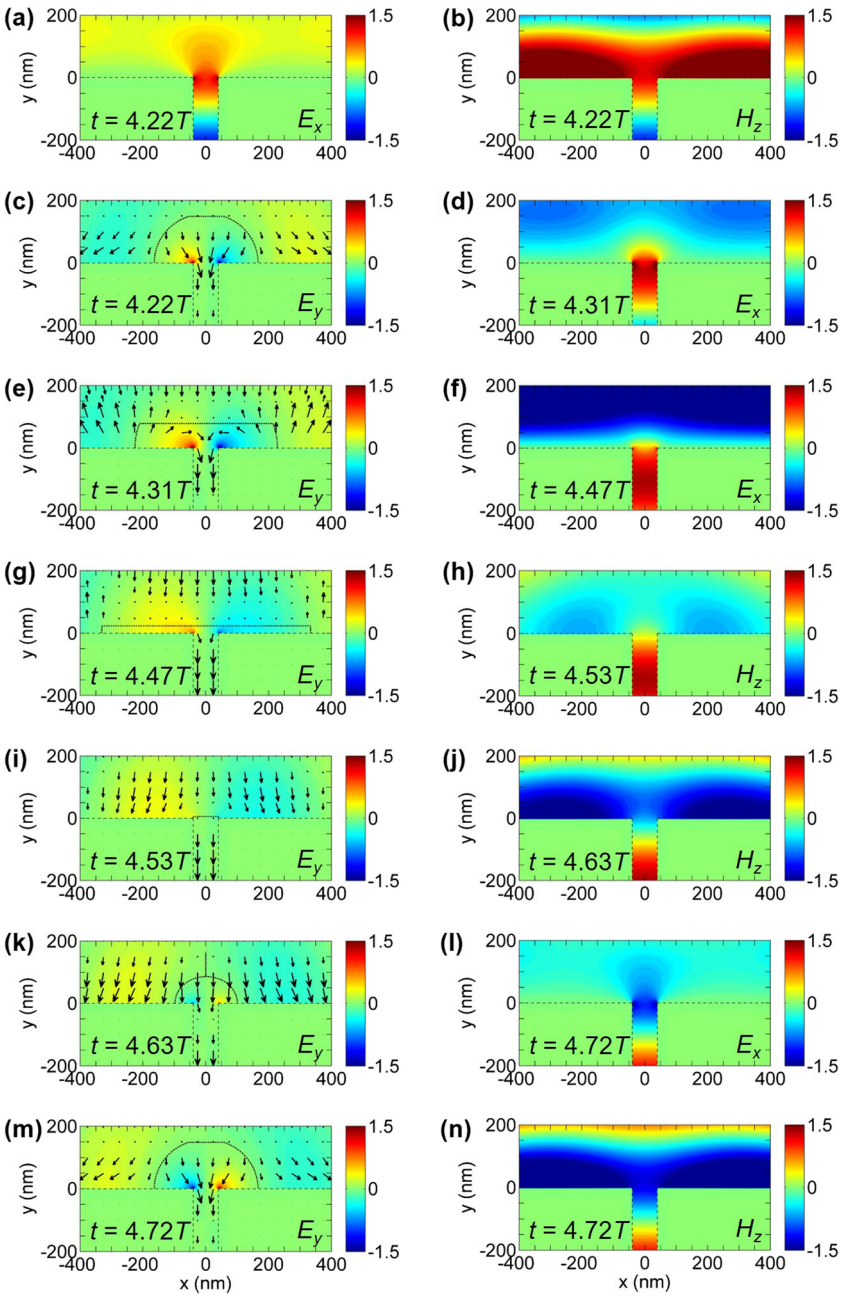

Fig. 2 Instant electric field and magnetic field from the simulation. The dashed lines indicate the boundary of the slit, and the dotted curves in **c**, **e**, **g**, **i**, **k**, and **m** indicate the instant funneling boundaries

propagate in the $\pm x$ direction. The Poynting vector is close to zero above the slit, and the funneling boundary becomes the widest. The energy transmitted at the entrance also becomes smaller.

The H_z field is shown in Fig. 2h as t continues to 4.53 T. The phase near the entrance is zero while that away from it is negative. The E_y field as shown in Fig. 2i indicates the field propagates further. But, no charges are accumulated. The Poynting vector in Fig. 2i is therefore deflected from the slit. The funneling boundary coincides with the entrance and the energy transmitted is about zero.

At $t = 4.64$ T, the H_z and E_y fields are shown in Fig. 2j, k, respectively. The phase of the H_z field at the entrance becomes negative. At this instant, charges are accumulated at both sides of the entrance. But at this time, the signs of the charges are interchanged in contrast to those shown in Fig. 2c. The Poynting vector shown in Fig. 2k indicates that the energy flows into the slit again, and the funneling boundary becomes larger. At $t = 4.72$ T, the E_x, H_z, and E_y fields are shown in Fig. 2i–n, respectively. Since it is 0.5 T later than that for the fields shown in Fig. 2a–c, the field distributions are similar but the phases become opposite. The Poynting vector and the funneling boundary are therefore the same as those shown in Fig. 2c. The flow of the energy and the variation of the funneling boundary repeat as discussed when t increases.

The normalized time-averaged Poynting vector in the x and y directions are obtained from

$$\langle S_x(x,y)\rangle = \frac{1}{S_0}\frac{1}{T}\int_{t_a}^{t_b} S_x(x,y,z)\mathrm{d}t, \tag{1a}$$

$$\langle S_y(x,y)\rangle = \frac{1}{S_0}\frac{1}{T}\int_{t_a}^{t_b} S_y(x,y,z)\mathrm{d}t, \tag{1b}$$

where $t_a = 4\ T$, $t_b = t_a + T = 5\ T$, and $S_0 = 1/2$ is the magnitude of the Poynting vector of the incident wave. The Poynting vector $\langle \mathbf{S}\rangle = \hat{x}\langle S_x\rangle + \hat{y}\langle S_y\rangle$ and its magnitude contour $|\langle \mathbf{S}\rangle| = (\langle S_x\rangle^2 + \langle S_y\rangle^2)^{1/2}$ are shown in Fig. 3. We obtain that the energy above and near the slit is funneled into the slit, while that away from the slit is deflected. Similar to the instant Poynting vector, we find the locations where $\langle S_x\rangle = 0$ along the x direction at every y to define the funneling boundary and show it in Fig. 3 as the dotted curve. Inside the boundary, the energy flows toward the slit. That is, the slit collects the nearby energy so that $|\langle \mathbf{S}\rangle|$ in the slit is larger than unity. In our case, we obtain that $|\langle \mathbf{S}\rangle|$ is uniform when $y << 0$ and is about 1.864.

Funneling Boundary Related to the Slit Width

The normalized energy flux of the wave transmitted through the slit is defined as

$$P = \frac{1}{w}\int_{-\frac{w}{2}}^{\frac{w}{2}} \langle S_y(x,y)\rangle \mathrm{d}x, \tag{2}$$

for $y < 0$. For $w < \lambda/2$, $\langle S_y\rangle$ in the slit is constant in the x direction since there only exists the fundamental mode [17]. Therefore, we obtain $P = \langle S_y\rangle$.

We change the slit width w in the simulation to obtain the normalized energy flux P and show the results in Fig. 4a. It is obtained that, when w decreases, P increases. When $w =$ 80, 160, and 240 nm, P is 1.864, 1.259, and 1.042, respectively. An exponent fitting function indicates that, when w approaches to zero, P approaches to a constant of four. Our simulation results are consistent to the previous studies of Refs. [23–25].

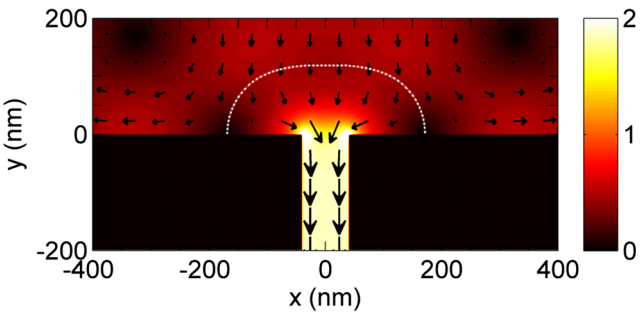

Fig. 3 Time-averaged Poynting vector and its magnitude contour. The dotted curve indicates the funneling boundary

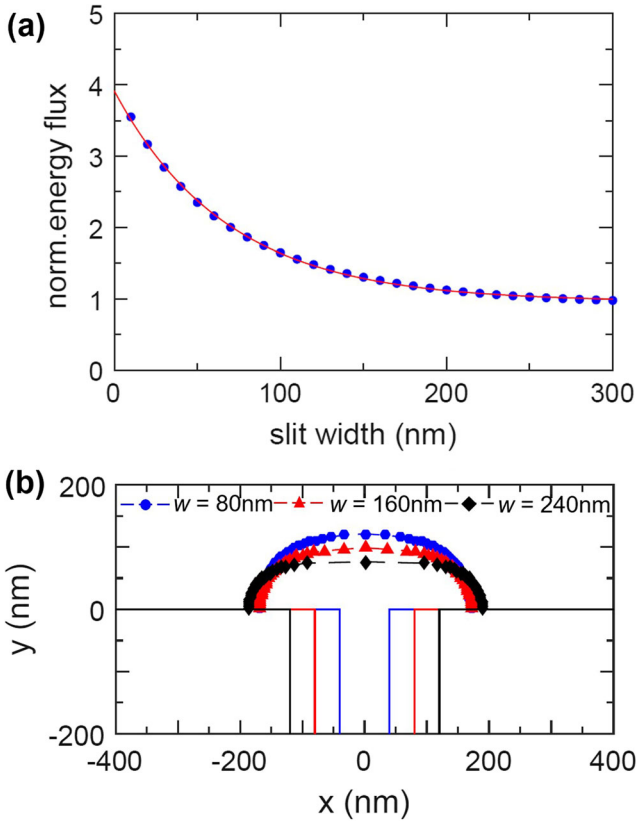

Fig. 4 **a** Transmitted energy flux normalized to the slit width (blue circles) and exponential fitting function $P(w) = 2.957\exp(-0.014w) + 0.961$ (red curve). **b** Funneling boundary obtained when $w = 80$ nm (blue circles), 160 nm (red triangles), and 240 nm (black diamonds). In **b**, the lines indicate the boundary of the various slit widths; blue lines: $w = 80$ nm, red lines: $w = 160$ nm, black lines: $w = 240$ nm

The funneling boundaries for the cases of $w = 80$, 160, and 240 nm are further shown in Fig. 4b. The width of the boundary remains about 340, 343, and 377 nm, respectively. However, the height of the boundary for the smallest $w = 80$ nm case is the largest 121 nm while those for the other two cases are 99 and 76 nm, respectively. The estimated funneling areas for the three widths are 3.388×10^4, 2.760×10^4, and 2.462×10^4 nm^2. This indicates that, while the narrower slit enhances P, it also enlarges the funneling area.

Light Funneling into a Subwavelength Slit of Finite Thickness

In this section, we consider a subwavelength slit in a PEC film of finite thickness h as shown in Fig. 5. When the incident

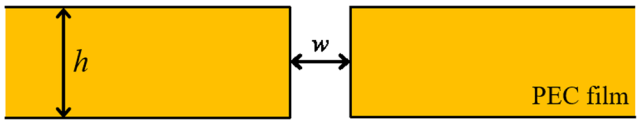

Fig. 5 Schematic of a subwavelength slit of width w and thickness h in a PEC film

wave is transmitted though the slit entrance, the wave propagates to the slit exit. It is reflected at the exit. Then, the reflected wave propagates back to entrance and is reflected again. The process repeats as the Fabry-Pérot resonance Refs. [17, 18, 36].

The film thickness h determines the phase difference between those of the incident and the reflected wave. The normalized energy flux P that is considered here is the energy of the total wave field. We show P as functions of the film thickness h in Fig. 6a for the cases of $w = 80$ nm, where h is varied from 200 to 800 nm in a step of 5 nm. The function is periodic, and the period is $\lambda/2 = 320$ nm, featured as the Fabry-Pérot resonance.

When $h = 545$ nm, $P = 2.575$ is at the second peak. The Fabry-Pérot resonance therefore enhances P as compared to the $w = 80$ nm case discussed in the previous section that only considers the light transmission through the slit entrance. According to Fig. 4a, the increasing ratio of P is $2.575/1.864 - 1 = 38.1\%$.

The corresponding light funneling boundary for the $h = 545$ nm case is shown in Fig. 6b. The width and the height become 386 and 114 nm, respectively, and the estimated funneling area is 3.686×10^4 nm^2. Although the height is slightly decreased when compared with the $w = 80$ nm case as what we showed in Fig. 4b, we obtain that the width of the boundary is notably increased; consequently, the area is $3.686 \times 10^4/(3.388 \times 10^4) - 1 = 8.8\%$ increased.

We further choose the case of $h = 385$ nm to study, where $P = 0.829$ in this case is at the first bottom of Fig. 6a. The energy flux P in this film thickness is $1 - 0.829/1.864 = 55.5\%$ decreased. The corresponding funneling boundary is shown in Fig. 6b. While the width and the height of the boundary are both significantly decreased to 221 and 89 nm, the funneling area is decreased to 1.541×10^4 nm^2; that is, the area has the $1 - 1.541 \times 10^4/(3.388 \times 10^4) = 54.5\%$ decrease.

We thus obtain the correspondence that the change of the funneling area is related to the change of the energy flux P. With the Fabry-Pérot resonance in the cases of the finite film thickness, the funneling area is enlarged with the increase of P, and vice versa. The correspondence suggests that the Fabry-Pérot resonance can enhance or reduce the slit capability of collecting and intensifying the light wave energy in the slit.

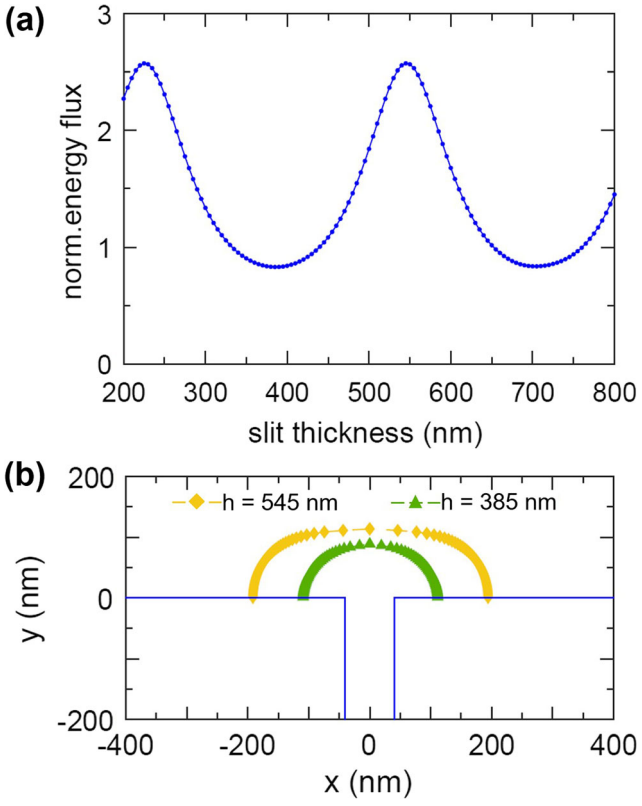

Fig. 6 **a** Transmitted energy flux normalized to the slit width $w = 80$ nm as a function of slit thickness. **b** Funneling boundary obtained when $h = 545$ nm (gold diamonds) and 385 nm (green triangles). In **b**, the blue lines indicate the boundary of the slit

Summary

In summary, we have shown the funneling mechanism of light transmission through the entrance of a subwavelength slit by the various instant EM fields from the FDTD simulation. The accumulated charge at the edges of the slit drew the light energy adjacent to the slit so that the transmitted energy was enhanced. We defined the boundary of the funneling profile according to the time-averaged Poynting vector in the x direction to explicitly indicate the area where the energy could be collected by the slit. As the normalized energy flux increased with the decrease of the slit width, we obtained that the funneling area was correspondingly increased. The finite slit thickness was considered to study the Fabry-Pérot resonance. At the thickness where the transmitted energy is enhanced, the funneling area was enlarged, and vice versa. Therefore, the slit capability of collecting the light was regulated by the resonance condition so that the funneling area was altered.

Acknowledgments The authors are grateful for support from Ministry of Science and Technology, Taiwan (MOST 104-2112-M-006-004-MY3) and computational resources at National Center for High-performance Computing (NCHC) of National Applied Research Laboratories (NARLabs) of Taiwan.

References

1. Ebbesen TW, Lezec HJ, Ghaemi HF, Thio T, Wolff PA (1998) Extraordinary optical transmission through sub-wavelength hole arrays. Nature 391(6668):667–669
2. Porto JA, García-Vidal FJ, Pendry JB (1999) Transmission resonances on metallic gratings with very narrow slits. Phys Rev Lett 83(14):2845–2848

3. Thio T, Pellerin KM, Linke RA, Lezec HJ, Ebbesen TW (2001) Enhanced light transmission through a single subwavelength aperture. Opt Lett 26(24):1972–1974
4. García-Vidal FJ, Martín-Moreno L (2002) Transmission and focusing of light in one-dimensional periodically nanostructured metals. Phys Rev B 66(15):155412
5. Lezec HJ, Degiron A, Devaux E, Linke RA, Martin-Moreno L, Garcia-Vidal FJ, Ebbesen TW (2002) Beaming light from a subwavelength aperture. Science 297(5582):820–822
6. García-Vidal FJ, Martín-Moreno L, Lezec HJ, Ebbesen TW (2003) Focusing light with a single subwavelength aperture flanked by surface corrugations. Appl Phys Lett 83(22):4500–4502
7. Martín-Moreno L, García-Vidal FJ, Lezec HJ, Degiron A, Ebbesen TW (2003) Theory of highly directional emission from a single subwavelength aperture surrounded by surface corrugations. Phys Rev Lett 90(16):167401
8. Chen KR (2010) Focusing of light beyond the diffraction limit of half the wavelength. Opt Lett 35(22):3763–3765
9. Chen KR, Chu WH, Fang HC, Liu CP, Huang CH, Chui HC, Chuang CH, Lo YL, Lin CY, Hwung HH, Fuh AYG (2011) Beyond-limit light focusing in the intermediate zone. Opt Lett 36(23):4497–4499
10. Yuan G, Rogers ETF, Roy T, Adamo G, Shen Z, Zheludev NI (2014) Planar super-oscillatory lens for sub-diffraction optical needles at violet wavelengths. Sci Rep 4:6333
11. Zhang X, Yan L, Guo Y, Pan W, Luo B, Luo X (2016) Enhanced far-field focusing by plasmonic lens under radially polarized beam illumination. Plasmonics 11(1):109–115
12. Anker JN, Hall WP, Lyandres O, Shah NC, Zhao J, Van Duyne RP (2008) Biosensing with plasmonic nanosensors. Nat Mater 7(6): 442–453
13. Novotny L, van Hulst N (2011) Antennas for light. Nat Photonics 5(2):83–90
14. Fang N, Lee H, Sun C, Zhang X (2005) Sub-Diffraction-Limited Optical Imaging with a Silver Superlens. Science 308(5721):534–537
15. Catrysse PB, Wandell BA (2003) Integrated color pixels in 0.18-μm complementary metal oxide semiconductor technology. J Opt Soc Am A 20(12):2293–2306
16. Xu T, Wu Y-K, Luo X, Guo LJ (2010) Plasmonic nanoresonators for high-resolution colour filtering and spectral imaging. Nat Commun 1:59
17. Takakura Y (2001) Optical resonance in a narrow slit in a thick metallic screen. Phys Rev Lett 86(24):5601–5603
18. Bravo-Abad J, Martín-Moreno L, García-Vidal FJ (2004) Transmission properties of a single metallic slit: from the subwavelength regime to the geometrical-optics limit. Phys Rev E 69(2): 026601
19. Xie Y, Zakharian A, Moloney J, Mansuripur M (2004) Transmission of light through slit apertures in metallic films. Opt Express 12(25):6106–6121
20. Lalanne P, Hugonin JP, Rodier JC (2005) Theory of surface plasmon generation at nanoslit apertures. Phys Rev Lett 95(26):263902
21. García-Vidal F, Moreno E, Porto J, Martín-Moreno L (2005) Transmission of light through a single rectangular hole. Phys Rev Lett 95(10):103901
22. Nikitin AY, Zueco D, García-Vidal FJ, Martín-Moreno L (2008) Electromagnetic wave transmission through a small hole in a perfect electric conductor of finite thickness. Phys Rev B 78(16): 165429
23. Sturman B, Podivilov E, Gorkunov M (2010) Transmission and diffraction properties of a narrow slit in a perfect metal. Phys Rev B 82(11):115419
24. Chang S-H, Su Y-L (2015) Mapping of transmission spectrum between plasmonic and nonplasmonic single slits. I: resonant transmission. J Opt Soc Am B 32(1):38–44
25. Chang S-H, Su Y-L (2015) Mapping of transmission spectrum between plasmonic and nonplasmonic single slits. II: nonresonant transmission. J Opt Soc Am B 32(1):45–51
26. Astilean S, Lalanne P, Palamaru M (2000) Light transmission through metallic channels much smaller than the wavelength. Opt Commun 175(4–6):265–273
27. Pendry JB, Martín-Moreno L, Garcia-Vidal FJ (2004) Mimicking surface plasmons with structured surfaces. Science 305(5685):847–848
28. Liu H, Lalanne P (2008) Microscopic theory of the extraordinary optical transmission. Nature 452:728–731
29. van Beijnum F, Rétif C, Smiet CB, Liu H, Lalanne P, van Exter MP (2012) Quasi-cylindrical wave contribution in experiments on extraordinary optical transmission. Nature 492:411–414
30. García-Vidal FJ, Lezec HJ, Ebbesen TW, Martín-Moreno L (2003) Multiple paths to enhance optical transmission through a single subwavelength slit. Phys Rev Lett 90(21):213901
31. Thomas DA, Hughes HP (2004) Enhanced optical transmission through a subwavelength 1D aperture. Solid State Commun 129(8):519–524
32. Shi H, Dong X, Lv Y, Du C (2009) Multi-interaction of surface wave between subwavelength grooves surrounding a single metallic slit. Appl Phys B Lasers Opt 95(2):345–350
33. Hong J-S, Chen K-R (2017) Light diffraction by a slit and grooves with a point source model based on wave dynamics. Phys Rev A 96(4):043813
34. Subramania G, Foteinopoulou S, Brener I (2011) Nonresonant broadband funneling of light via ultrasubwavelength channels. Phys Rev Lett 107(16):163902
35. Goncharenko AV, Kim KY, Hong J-S, Chen K-R (2012) Complex mechanism of enhanced optical transmission through a composite coaxial/circular aperture. Plasmonics 7(3):417–426
36. Hong J-S, Chen AE, Chen K-R (2015) Modulated light transmission through a subwavelength slit at early stage. Opt Express 23(8): 9901–9910
37. Bouchon P, Pardo F, Portier B, Ferlazzo L, Ghenuche P, Dagher G, Dupuis C, Bardou N, Haïdar R, Pelouard J-L (2011) Total funneling of light in high aspect ratio plasmonic nanoresonators. Appl Phys Lett 98(19):191109
38. Zhu P, Jin P, Shi H, Guo LJ (2013) Funneling light into subwavelength grooves in metal/dielectric multilayer films. Opt Express 21(3):3595–3602
39. Sounas DL, Alù A (2016) Color separation through spectrally-selective optical funneling. ACS Photonics 3(4):620–626
40. Wuenschell J, Kim HK (2008) Excitation and propagation of surface plasmons in a metallic nanoslit structure. IEEE Trans Nanotechnol 7(2):229–236
41. Xi Y, Jung YS, Kim HK (2010) Interaction of light with a metal wedge: the role of diffraction in shaping energy flow. Opt Express 18(3):2588–2600
42. Pardo F, Bouchon P, Haïdar R, Pelouard J-L (2011) Light funneling mechanism explained by magnetoelectric interference. Phys Rev Lett 107(9):093902
43. Adams DC, Inampudi S, Ribaudo T, Slocum D, Vangala S, Kuhta NA, Goodhue WD, Podolskiy VA, Wasserman D (2011) Funneling light through a subwavelength aperture with epsilon-near-zero materials. Phys Rev Lett 107(13):133901
44. Betzig E, Harootunian A, Lewis A, Isaacson M (1986) Near-field diffraction by a slit—implications for superresolution microscopy. Appl Opt 25(12):1890–1900